The effect of tip clearance on the rotor-stator interaction and noise of marine 1.5-stage compressor

Huabing Lu [a,b], Youhong Xiao [a,*], Zhigang Liu [a], Ye Yuan [a], Peilin Zhou [b,*]
[a] College of Power and Energy Engineering, Harbin Engineering University, Harbin, China.
[b] Department of Naval Architecture, Ocean & Marine Engineering, University of Strathclyde, Glasgow, United Kingdom.

Abstract

Tip-clearance (TC) noise is significant in compressors and has garnered scholarly attention for the isolated rotor. However, applying these findings to marine compressors with rotor-stator-interaction (RSI) is challenging. In this paper, a comprehensive analysis was given of a marine 1.5-stage compressor. The investigation included five different TC configurations (0, 0.25, 0.5, 0.75, and 1 mm) and the RSI was a focal point of the study. The accuracy of numerical calculations of the flow field was verified using experimental data. The results reveal a new phenomenon; the radial separation flow of the rotor's trailing edge is mixed with the TC flow and a wake above the 90 span of the blade is formed. An understanding of this mixing mechanism is crucial for model that describes the effect of TC on the RSI. The single-tone sound source of the stator's leading-edge tip area is the smallest when the TC is 0.25 mm. In contrast, the single-tone sound source is largest when the TC is equal to zero. Investigation of different TCs in three acoustic environments shows no obvious disparity in the single-tone acoustic power response of various TCs. There is, however, a correlation between the flow mixing mechanism and the noise.

This is a peer-reviewed, accepted author manuscript of the following research article: Lu, H., Xiao, Y., Liu, Z., Yuan, Y., & Zhou, P. (2023). The effect of tip clearance on the rotor-stator interaction and noise of marine 1.5-stage compressor. *Journal of Marine Engineering & Technology*, 1-14. https://doi.org/10.1080/20464177.2023.2255337

Keywords：Marine 1.5-stage compressor; Tip clearance noise; Rotor-stator interaction; Single-tone noise

1. Introduction

A pivotal role is assumed by gas turbines across a spectrum of engineering domains encompassing aeronautics, space exploration, thermal power generation, and notably, maritime transportation. A commensurate elevation in the aerodynamic noise resultant from ship gas turbine operations has been witnessed in the context of an accelerated surge in the requisition for high-power and high-speed propulsion systems within maritime vessels. The intensifying acoustic characterization has engendered the enactment of rigorous regulations by international classification societies, with the objective of preempting human exposure to potentially perilous noise thresholds within onboard living and operational environments. Consequently, impetus is directed towards the pursuit of research concerning noise emanations from marine gas turbines, accentuating a particular focus on the acoustic emissions that originate from fan or compressor components. These constituents are conjectured to fundamentally govern the comprehensive auditory milieu propagated into the contiguous cabin surroundings.

There are many studies on noise reduction measures for compressor sound sources. The most successful noise reduction measure was described by the pipe acoustic mode theory proposed by Tyler and Sofrin (Tyler and Sofrin 1962); By rationally selecting the number of rotors and stators, the tonal noise mode of the rotor-stator-interaction (RSI) was "cut-off" in the tube. This selection technique has become the basic principle in the low-noise design of turbomachines. It has also been shown that the design of the (i) rotor-stator gap (Canepa et al. 2013; Canepa et al. 2015), (ii) sweep and lean of the stator (Envia et al. 1996; Zhang W et al. 2017; Cheng et al. 2019; Ghodake et al. 2019; Sanders et al. 2020), and (iii) wavy leading or trailing edge blades (Tong et al. 2018; Yang Y et al. 2020) were effective methods for noise reduction in compressors.

Kameier and Neise (Kameier and Neise 1997) showed that the noise caused by the secondary flow in the rotor’s tip clearance (TC) was an important source in impeller machinery. The influence of TC leakage on the internal flow field of turbomachinery has been studied and numerous scholars have conducted in-depth studies on instability. Zhang et al. (Zhang B et al. 2021) pointed out that large clearance leakage flow was the main reason for the rotational stall of transonic compressors and the aerodynamic performance of the compressor was improved when the TC was halved. Hah et al. (Hah et al. 2006) found that when the compressor worked near the stall, the TC vortex oscillated and caused large pressure fluctuations at the rotor end wall. Afterward, the researchers investigated the effect of TC changes on compressors. Du et al. (Du et al. 2008) studied the TC flow stability under three different TCs for the NASA Rotor 67. The results showed that the larger the TC, the larger the influence range and instability of the tip leakage flow. Zhang et al. (Zhang H et al. 2005) observed similar behavior in isolated compressor rotors. Zhang et al. (Zhang M et al. 2021) conducted an experimental study on a low-speed, single-stage fan and demonstrated that the TC can be optimized to maximize the mass flow range.

The contribution of the TC flow to the aerodynamic noise of turbomachinery has also been the subject of investigations. Canepa et al. (Canepa et al. 2019) carried out experimental research on a low-speed axial fan using particle image velocimetry (PIV) technology and acoustic measurements. Their results showed that TC flow made a significant contribution to the sound pressure level (SPL) spectrum and this contribution increased with the blade load. Through experiments and numerical methods, Zhu et al. (Zhu et al. 2018) found that there were narrow-band peaks related to the TC in the acoustic spectrum of an isolated axial fan. Further studies confirmed that the narrow-band peaks were generated by the interaction of coherent flow structures in the blade tip region and the leading edge. Nevertheless, studies by others had come to disparate conclusions. Galindo et al. (Galindo et al. 2015) analyzed the aerodynamic and noise characteristics of centrifugal compressor tip leakage flow based on numerical methods. Under the near-surge condition, the TC was in the strong backflow region and the tip leakage couldn’t establish any coherent noise source mechanisms.

Some scholars have paid attention to the control strategies of TC noise, but few relevant pieces of literature have been found. The TC flow is determined by the clearance pressure difference, clearance size, and flow resistance, which undoubtedly indicates the research direction of TC noise control (Zhang C, Ji, Zhou, Sun 2020). Some investigations have changed the configuration of the isolated fan TC structure including, e.g., adding annular protrusions to the inner casing wall (Zhu and Carolus 2018), adding end-plates to the fan tip (Corsini et al. 2009), blended blade tip and winglet technology (Zhang C, Ji, Zhou, Sun 2020; Zhang C, Ji, Zhou, Zhang 2020), boundary layer purging (Kornilov 2015), and swept blades (Boulamatsis et al. 2019). These measures suppressed the strength of the blade tip leakage vortex, reduced the fan's aerodynamic loss, and achieved the purpose of reducing the blade tip leakage noise. Furthermore, some researchers have explored the influence of different blade TCs on the fan's aerodynamic noise. Moghadam et al. (Moghadam et al. 2019) combined large eddy simulation (LES) and acoustic perturbation equations (APE) to numerically analyze the axial fan and the results showed that increasing the TC size would generate multiple vortices, increase the strength of the main tip vortex, and lead to a higher frequency sound field. Karstadt et al. (Karstadt et al. 2010) measured the noise characteristics of axial fans with five diverse TCs and found that the reduction in the TC resulted in lower aerodynamic noise. Wang et al. (Wang et al. 2020) carried out a numerical study on a single-stage fan and obtained similar conclusions. The increase of the blade TC would lead to a rise in the single-tone noise, but it had little effect on the radiation intensity of high-order harmonic noise. Avallone et al. (Avallone et al. 2020) have given detailed research results. In the noise study of wind turbines, the increase of the TC raised the noise in the axial direction but decreased the noise in the small-angle direction.

The relationship between the diverse TCs and fan noise has been investigated in previous studies. Most of the numerical investigations, however, have focused on axial fans with isolated rotors. Once the research object is changed to the compressor of gas turbines employed in ship, where the marine compressor has multiple rows of blades, the conclusions for the axial fans with isolated rotors are no longer applicable. Consequently, a comprehensive exploration of the impact of various TCs on rotor-stator interaction has yet to be extensively conducted within the existing literature. Moreover, a specific examination of the inherent flow mechanism generating noise in various TCs is notably absent. This critical research gap significantly hampers the understanding of noise generation mechanisms within multi-row impellers, particularly in the context of marine gas turbine engines encompassing multi-stage compressors and turbines. In this paper, we aimed to investigate the noise radiation characteristics and discuss the RSI of a marine 1.5-stage compressor with various TCs. Furthermore, the noise radiation characteristics of various TCs in free-field, infinitely long ducts, and actual ducts were studied in detail, and the excitation states of acoustic modes in infinitely long ducts were discussed. The analysis will ultimately contribute to the advancement of marine compressors characterized by reduced noise emissions, thereby furnishing technical guidance aimed at extending the design applicability to multi-stage axial compressors.

2. Numerical investigation of the flow field

2.1 Description of the marine compressor

The 1.5-stage compressor investigated in this study was based on the design of equipment used for marine gas turbines as shown in Figure 1. The through-flow of the compressor includes a horn-shaped inlet, mass flow tube, impeller, and an exhaust volute. Even though the compressor is axial, the exhaust volute still exists because the compressor requires an electric motor in the axial direction to drive the compressor. The exhaust volute, horn-shaped inlet, and mass flow tube do not participate in the pressurization process of the gas. The impeller is, therefore, the focus of aerodynamic research. The parameters listed in Table 1 define the impeller’s geometry, which includes three rows of blades (Figure 1).

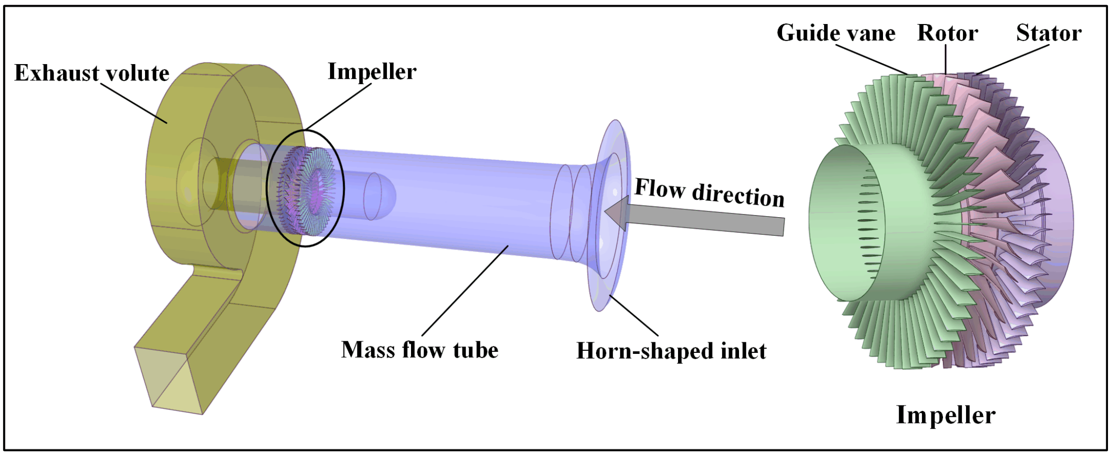

Figure 1. The configuration of the marine 1.5-stage axial compressor (left) and its impeller (right).

Table 1. Geometric parameters of the impeller.

Inlet/Outlet shroud diameter	458.4 mm
Inlet hub diameter	243.6 mm
Outlet hub diameter	279 mm
Number of guide vanes	54
Number of rotor blades	37
Number of stator blades	60
Tip clearance	0.5 mm

2.2 Axial compressor grid

Considering that the number of blades studied in this paper is large and the unsteady flow field calculation of five compressors with different TCs is required, a full-channel numerical simulation represents an insurmountable computational challenge. To simplify this problem, a 2:1:2 guide vane-rotor-stator channel number was applied for numerical simulations. The accuracy of the simulations is discussed in section 2.4. The computational domain and the number of channels are shown in Figure 2. The inlet and outlet were extended upstream and downstream from the blade positions to ensure stable airflow. The computing areas were divided into structured grids, as shown in Figure 3.

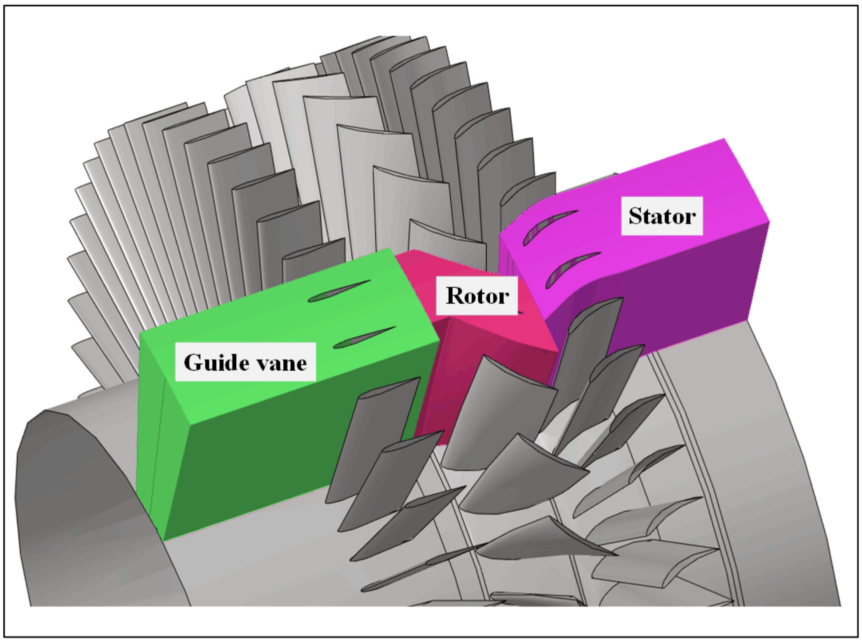

Figure 2. Compressor computation domains and the number of channels.

The focus of this paper is on the TC flow. To accurately simulate the flow around the TC area, there must be a sufficient number of grid layers to simulate the structure of the TC vortex. According to the results in the literature (Wang et al. 2020), this requires at least 15 grid layers for a TC below 2 mm. In this study, five different TCs (0, 0.25, 0.5, 0.75, and 1 mm) were used and the number of grid layers was set equal to 20 for all simulations, as shown in Figure 4. Perfectly matched grids were used on both sides of the TC area to avoid errors caused by the data exchange of mismatched grids.

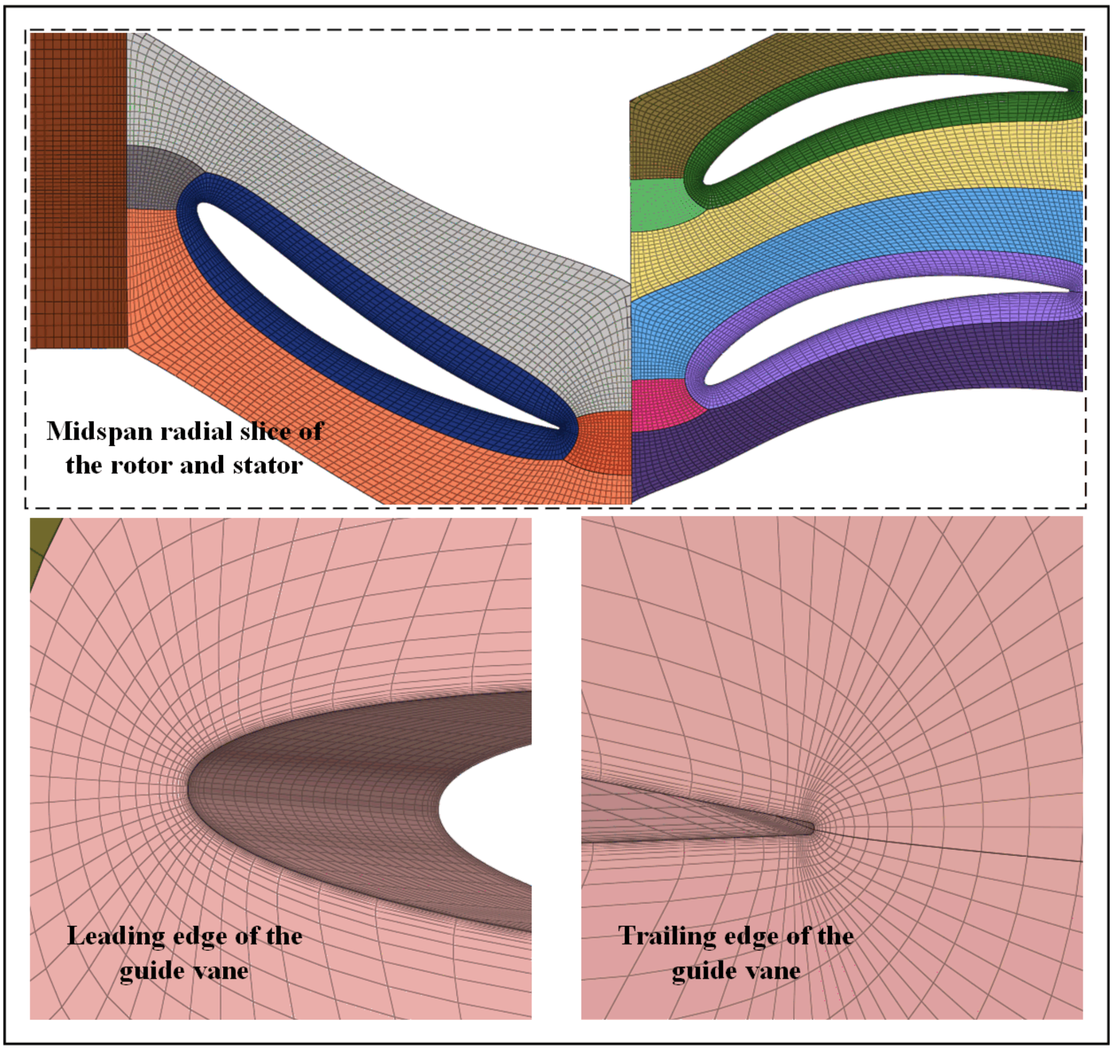

Figure 3. Radial slice grid of the rotor and stator (top) and guide vane leading and trailing edge grids (bottom).

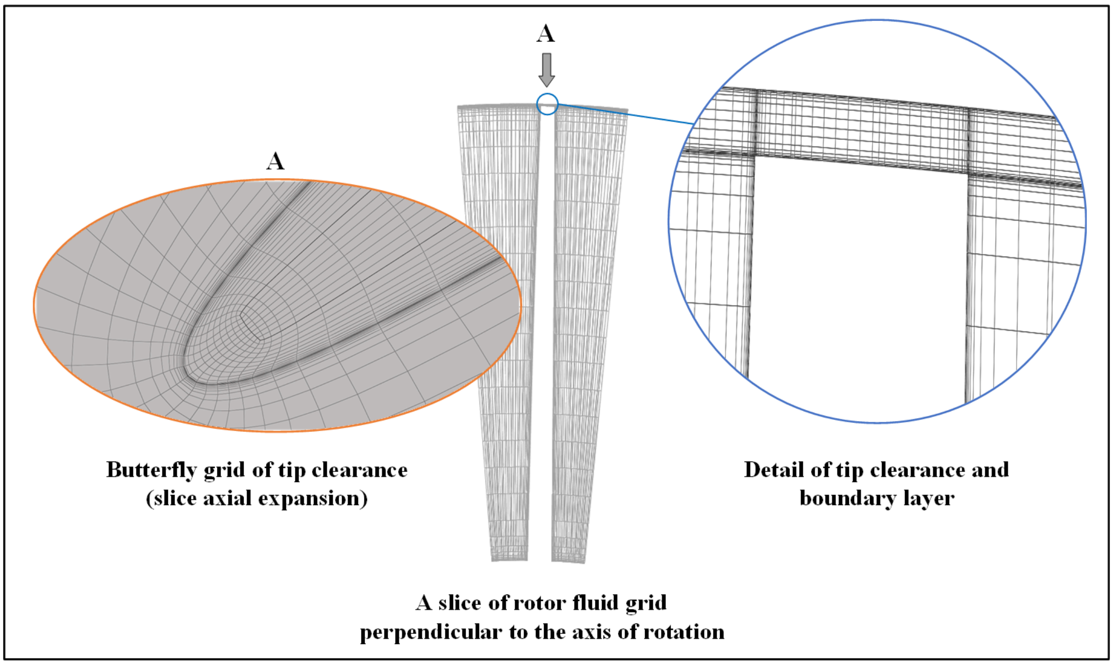

Figure 4. A slice of the rotor fluid and TC grid.

The numerical simulation of the flow field must meet certain accuracy requirements and reduce the computational cost as much as possible. Grid independence verification is, therefore, essential. For the design value of the TC of 0.5 mm, three sets of grids were applied used for numerical calculations, as detailed in Table 2. The difference between Case 2 and Case 3 is quite small and it can be concluded that the grid used in Case 2 is satisfactory.

Table 2. 1.5-stage axial compressor grid independence verification.

Number	Number of grids	Mass Flow (kg/s)	Pressure ratio	efficiency (%)
Case 1	899840	3.8017	1.0110	84.756
Case 2	2028032	3.8104	1.0111	84.919
Case 3	3354624	3.8124	1.0111	85.012

2.3 Setup of numerical simulation

The calculation of the numerical model was implemented using the CFX commercial code and the SST turbulence model was employed. The SST model is suitable for turbomachinery and can accurately predict the separation phenomenon of adverse pressure gradients on the blade surface (Yang J and Wu 2014; Shi et al. 2019). Pressure pulsations on the blade surface dominate the dipole sound source of the aerodynamic noise of subsonic impellers, which means that the SST turbulence model can also be applied in the calculation of the aerodynamic noise of turbomachinery.

To obtain accurate flow field results and aerodynamic sound sources, the turbulence format was set to second-order backward Euler and the convection format and turbulence accuracy were both high resolution. The compressor speed was set to 2270 rpm and the unsteady time step was defined as 40 steps of rotation of a single rotor channel, which corresponds to 1.78593×10^{-5} s. To ensure that the unsteady calculation of the compressor was easier to converge, the result of the steady calculation was adopted as the initial field of the unsteady calculation.

2.4 Experimental verification

The accuracy of numerical investigations was verified using a series of experimental measurements. The performance of the marine compressor was measured on the 1.5-stage subsonic compressor test platform, as shown in Figure 5, at the Harbin Engineering University. The compressor's performance was determined by measuring a series of thermodynamic parameters with a fixed throttle opening and rotor speed. These parameters include the total pressure, total temperature, and mass flow and were measured at the locations shown in Figure 6. Two different flowmeters were placed in sections A and B, which offered a useful comparison and verification of each measurement. Two three-hole comb total pressure probes were placed in sections C, D, E, and F, and there were two total temperature probes in section C. Section G contained a total temperature sensor used to measure the total temperature at the compressor outlet.

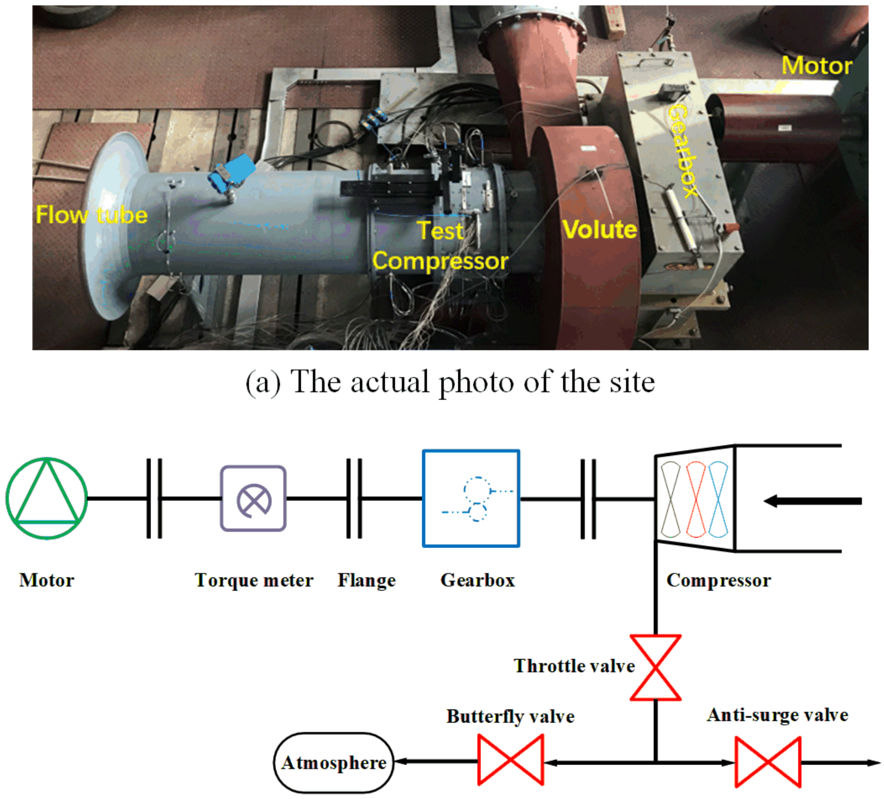

(a) The actual photo of the site

(b) The schematic diagram of the test bench equipment

Figure 5. Configuration of the marine compressor test bench.

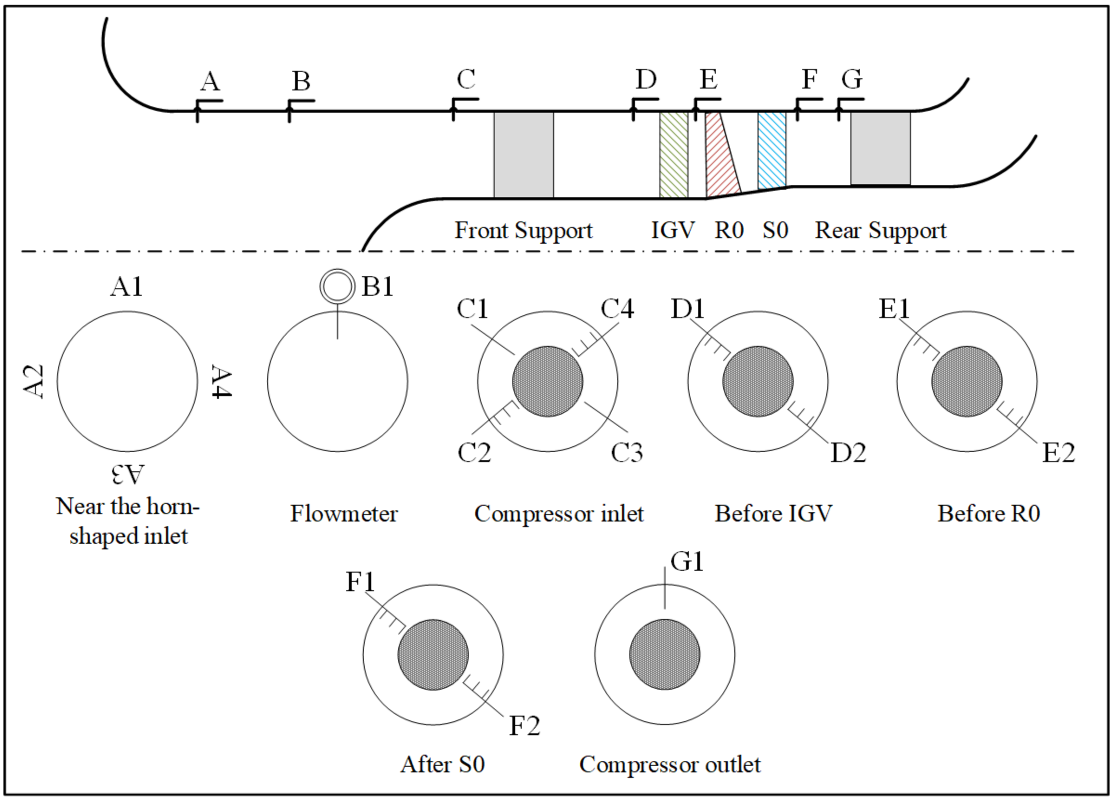

Figure 6. Measurement locations on the marine compressor test bench.

The measurements were used to determine the compressor's pressure ratio π and efficiency Eff according to equations (1) and (2). The relative error of the experimental and numerical data was quantified by the relative deviation ε, defined in equation (3).

$$\pi = \frac{P_{out}}{P_{in}} \tag{1}$$

$$Eff = \frac{\pi^{\frac{k-1}{k}} - 1}{T_{out} / T_{in} - 1} \tag{2}$$

$$\varepsilon = \frac{\left|\theta_{num} - \theta_{\exp}\right|}{\theta_{\exp}} \tag{3}$$

The overall performance and relative error of the compressor obtained from the numerical and experimental results are shown in Table 3. For a rotor speed of 2270 rpm with a TC of 0.5 mm, the numerical simulation and experimental results are in good agreement. This agreement shows that the use of the simplified 2:1:2 channel in the simulations is sufficiently accurate.

Table 3. The overall performance and relative error of the compressor, as obtained from numerical simulations and experiments.

Results	π	Eff (%)	ε_{π} (%)	ε_{Eff} (%)
Experimental	1.0089	84.916	–	–
Numerical	1.0111	84.919	0.218	0.004

3. Aerodynamic Noise Solutions

3.1 Aeroacoustic theory

The variational form of the Lighthill equation is used for compressor noise prediction. The Lighthill equation is given by(Lighthill 1952)

$$\frac{\partial^2 \rho_a}{\partial t^2} - a_0^2 \frac{\partial^2 \rho_a}{\partial x_i \partial x_i} = \frac{\partial^2 T_{ij}}{\partial x_i \partial x_j}, \tag{4}$$

where a_0 is the speed of sound, ρ_a is the density pulsation, and T_{ij} is the Lighthill stress tensor. After frequency domain transformation this becomes

$$-\omega^2 \rho_a - a_0^2 \frac{\partial^2 \rho_a}{\partial x_i \partial x_i} = \frac{\partial^2 T_{ij}}{\partial x_i \partial x_j}. \tag{5}$$

Introducing the potential function ψ and applying the weighted residual method variation gives

$$\frac{\omega^2}{a_0^2}\psi + \frac{\partial^2 \psi}{\partial x_i \partial x_i} = \frac{1}{i\omega} \frac{\partial^2 T_{ij}}{\partial x_i \partial x_j}. \tag{6}$$

The weak variational form associated with equation (6) can be written as

$$-\int_{\Omega} \frac{\omega^2}{\rho_0 a_0^2} \psi \delta\psi \, d\Omega - \int_{\Omega} \frac{1}{\rho_0} \frac{\partial \psi}{\partial x_i} \frac{\partial \delta\psi}{\partial x_i} d\Omega = S_{\Omega} + S_{\Gamma}, \tag{7}$$

where S_{Ω} and S_{Γ} are given by

$$S_{\Omega}=\int_{\Omega}\frac{i}{\rho_0\omega}\frac{\partial\delta\psi}{\partial x_i}\frac{\partial T_{ij}}{\partial x_j}d\Omega \tag{8}$$

and

$$S_{\Gamma}=-\int_{\Gamma}\frac{\delta\psi}{i\rho_0\omega}\frac{\partial}{\partial x_i}\left(a_0^2\rho_a\delta_{ij}+T_{ij}\right)n_i d\Gamma . \tag{9}$$

S_{Ω} and S_{Γ} represent the contribution of volume and surface sound sources, respectively. Further detail on the variational form of Lighthill's analogy is given by Oberai et al. (Oberai et al. 2000, 2002)

3.2 Noise prediction scheme

The variational form of Lighthill was adapted for the finite element method (FEM) and acoustic calculations were implemented using the MSC ACTRAN code. The fluid information such as velocity was mapped to the acoustic grid and then converted into aerodynamic sound sources using Lighthill's variational form theory. Finally, noise prediction was performed on the finite element grid. A flow diagram of the aerodynamic noise prediction process based on the computational fluid dynamics (CFD) results is shown in Figure 7.

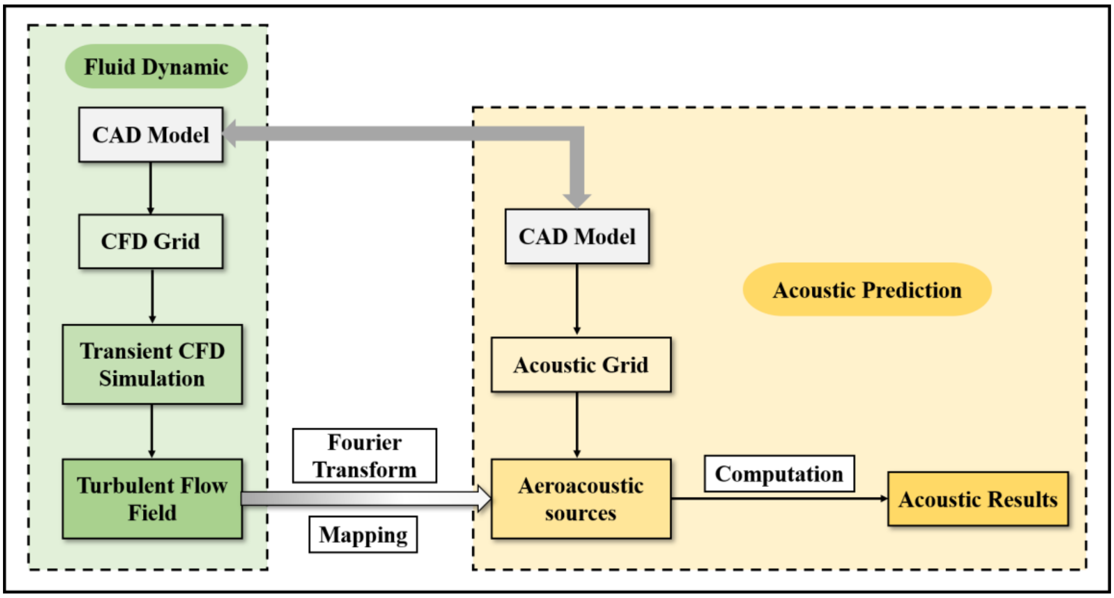

Figure 7. Flow diagram of the noise prediction process based on CFD results.

The direct indicators of machine noise intensity are undoubtedly the radiated sound power in free-field in noise analysis, which not involve complex structures that can reflect or diffract noise, thereby providing a direct representation of the noise generated under different TCs. Furthermore, the acoustic response of an actual machine within an infinitely long duct is intricately connected to the acoustic mode of the duct. The analysis of noise response within such duct serves as a foundational approach to comprehend sound propagation tendencies within actual ducts. Simultaneously, the acoustic analysis conducted within the infinitely long duct serves as a valuable complement, enriching the depiction of the compressor's noise characteristics under various TCs from diverse perspectives.

As a result, three sets of acoustic grids were created to explore the noise profile in three acoustic environments with different TCs, as shown in Figure 8. The free sound field, infinitely long duct, and actual duct correspond to Figures 8 (a), (b), and (c), respectively. The piping in (c) was modeled according to the compressor configuration shown in Figure 1, with the exhaust volute, horn-shaped inlet, and mass flow tube considered. Area A showed the fluid calculation area and the location of the aerodynamic sound source. The left and right end faces in (b) were applied with non-reflection pipe modes. The surfaces labeled B in (a) and (c) were non-reflective.

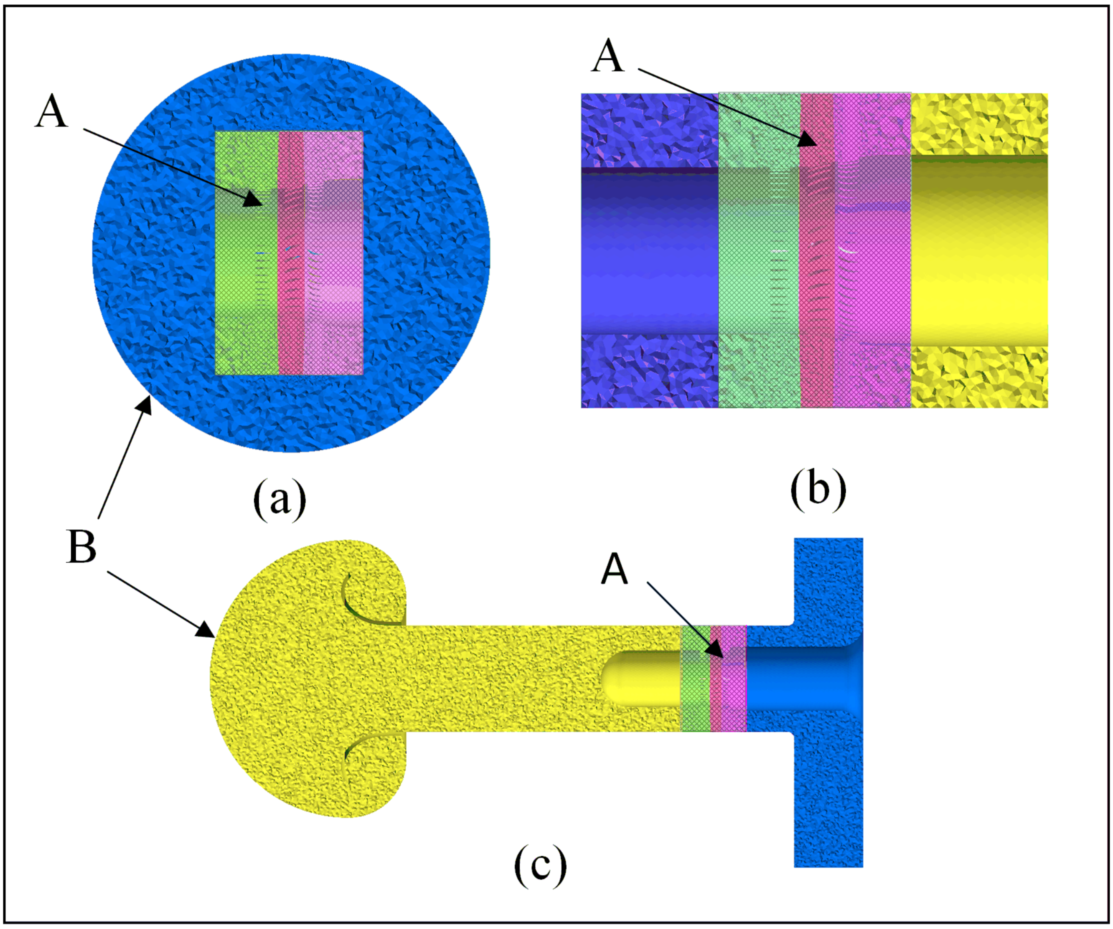

Figure 8. Three sets of acoustic grids corresponding to three acoustic environments, where (a) represents the free sound field, (b) represents the infinitely long duct, and (c) represents the actual duct.

For rotating machinery, the single-tone noise corresponding to the blade passing frequency (BPF) is the most significant(Polacsek et al. 2006) and the first three orders of the BPF should be considered. The BPF and its harmonic frequencies are given by equation (10)

$$f = \frac{nBi}{60}, \tag{10}$$

where n is the rotor speed, B is the number of rotor blades, i is the harmonic order, and f is the blade passing frequency. The third order BPF for the compressor studied here is 4200 Hz and the maximum frequency of interest for this paper was, therefore, set equal to 5000 Hz. There have been many studies on the size of the acoustic grid required for noise calculation (Hu et al. 2013; Zhang J et al. 2016), which have shown that it is often necessary to ensure that there are six elements within the wavelength of the highest frequency noise. The three sets of grids shown in Figure 8 contained eight elements within the wavelength of the highest frequency noise and, therefore, satisfy the requirements for the minimum grid number. The corresponding grid numbers are shown in Table 4.

Table 4. The grid number of the three sets of acoustic grids shown in figure 9.

Scenario	(a)	(b)	(c)
Number	5573299	4112663	11967292

4. Results and discussion

4.1 Influence of TC on the overall performance of the compressor

Table 5 gives an overview of the characteristics of the compressor for different TC conditions, including values for the unsteady time-averaged mass flow M , pressure ratio π , and efficiency Eff . Increasing the TC reduces the mass flow and efficiency, whilst the pressure ratio does not significantly change due to the low rotational speed. Increasing the TC from 0 to 1 mm corresponds to a decrease of about 1 % in mass flow and efficiency. Compared with the values presented in Table 3, the efficiency with TC set equal to 0.5 mm is slightly different, which is thought to be caused by the differences between the unsteady time-averaged results and the steady-state calculations.

Table 5. The overall characteristics of the compressor for five TC configurations.

TC (mm)	M (kg/s)	π	Eff (%)
0	3.8177	1.0109	85.832
0.25	3.8115	1.0109	85.596
0.5	3.8007	1.0108	85.318
0.75	3.7925	1.0108	84.972
1	3.7830	1.0108	84.786

To explore the effect of various TCs on the flow in the rotor tip region, the instantaneous static entropy distribution was calculated and is shown in Figure 10. Increasing the TC increases the range and strength of the tip leakage vortex, as indicated by the red arrows in the figure. No leakage vortices are found in the channel with TC = 0 mm. For TC = 1 mm, however, the tip leakage flow develops downstream in the channel and influences the pressure surface of the adjacent blades. Long-range, intense tip leakage vortices result in higher compressor losses, which explains the results summarized in Table 5.

The black circle in Figure 9 is the radial separation flow of the rotor suction surface. The extent of the radially separated flow becomes larger as it approaches the trailing edge of the blade. When TC is non-zero, radial separation flow and tip leakage flow will mix near the trailing edge of the blade, as shown in Figure 10. The larger the TC, the faster the mixing time. The white and green lines represent tip leakage flow and radially separated flow, which are blended at the trailing edge. The wake above the 90 span of the blade is thus generated, which is the main mechanism responsible for the effect of the TC on RSI.

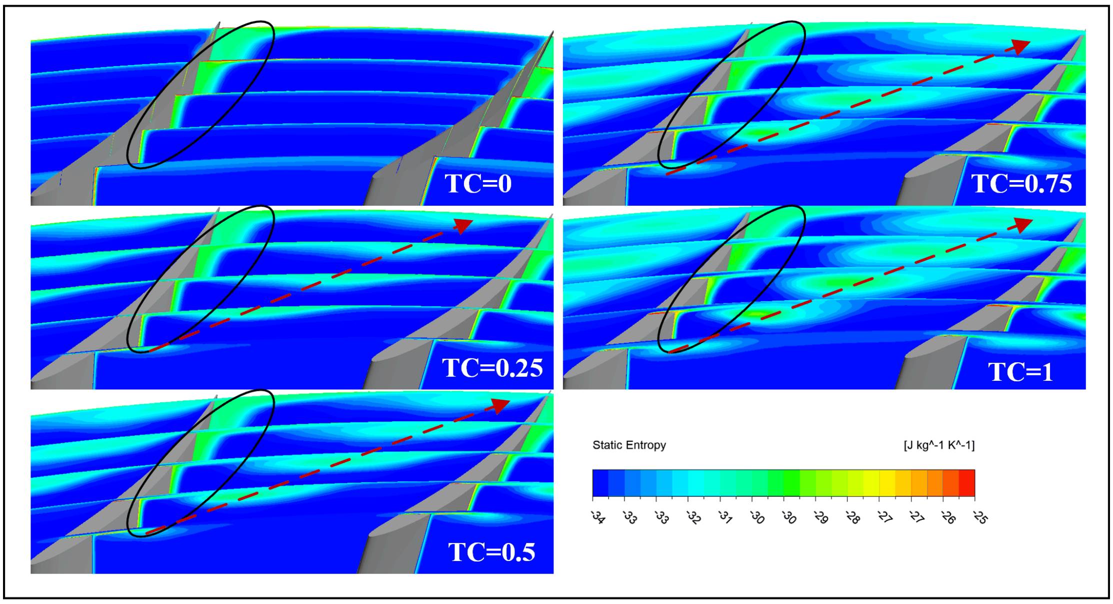

Figure 9. Instantaneous static entropy distribution in the rotor TC region.

The static pressure distribution of 99.8% span with TC = 1 mm is shown in Figure 11. Both sides of the rotor have high and low-pressure regions and the airflow near the TC mainly crosses the blade from the front half chord into the adjacent channel, as shown by the arrows in Figure 11.

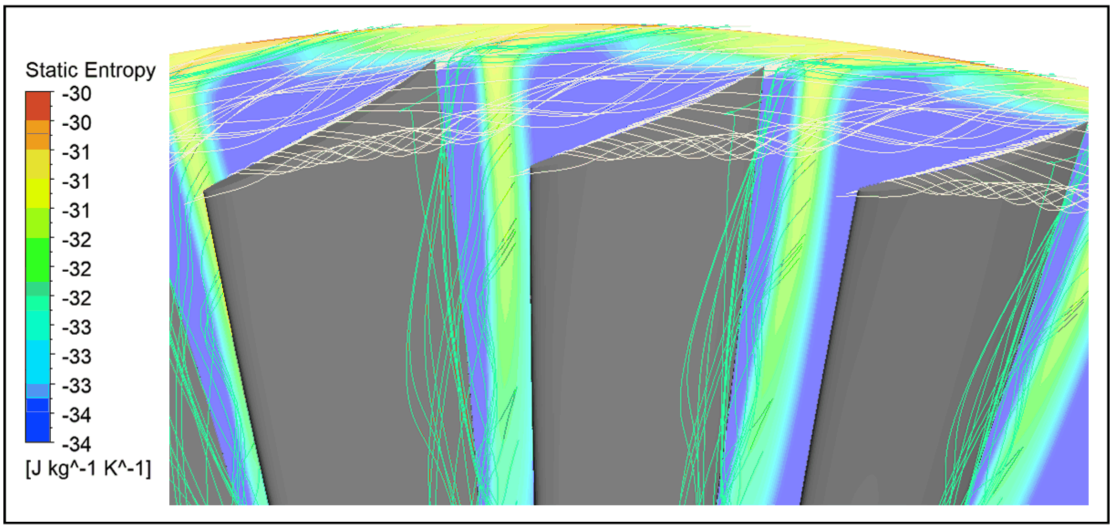

Figure 10. Flow structure and rotor wake composition.

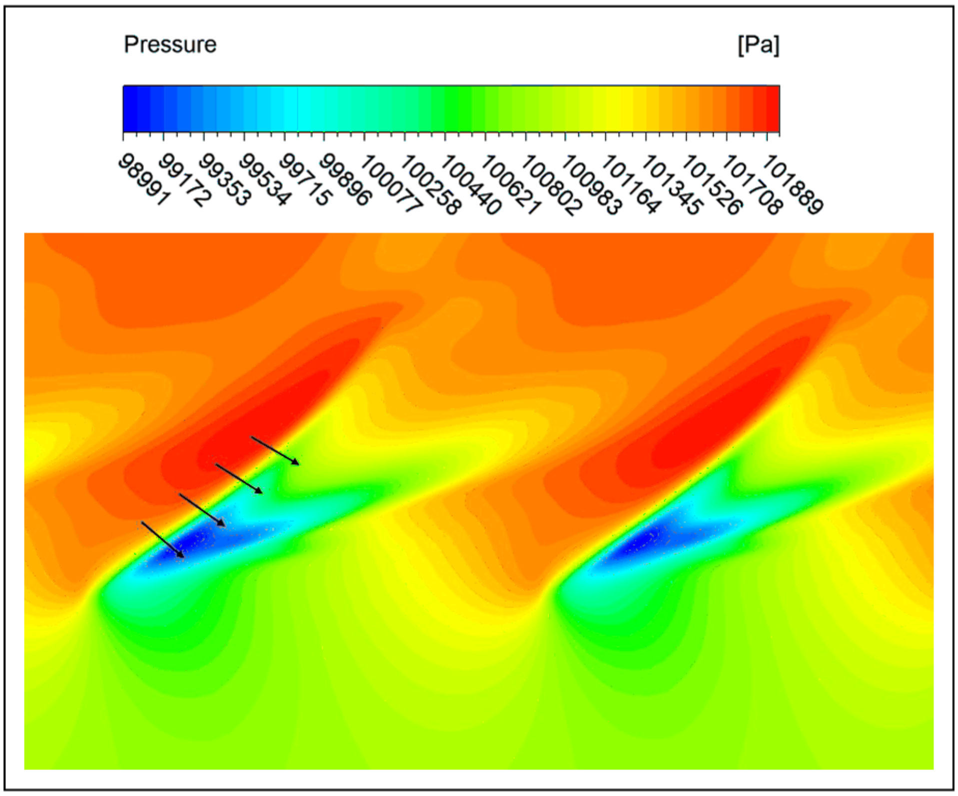

Figure 11. 99.8% span static pressure distribution and leakage flow direction with TC = 1 mm.

4.2 Influence of TC on the RSI

RSI is the basic mechanism of turbomachinery BPF noise generation (Tyler and Sofrin 1962). The rotor wake periodically impinges on the stator blades, producing large-scale unsteady pressure pulsations on the stator's surface (Goldstein 1976). To investigate this effect in this study, the unsteady pressure on the stator surface was extracted and the discrete Fourier transform (DFT) was applied to obtain the characteristics of the pressure amplitude in the frequency domain. Figure 12 shows the distribution of the pressure amplitudes on the stator surface for the first three orders of the BPF, calculated with a TC of 1 mm. The position of the largest pressure amplitude at the BPF and harmonic frequencies is on the leading edge of the blade, which also indicates that the leading edge is the most vital sound source related to the RSI. Similar conclusions were obtained by the numerical prediction based on LES by Lewis et al. (Lewis et al. 2022). There is also a large sound source region on the stator suction surface, which originates from the separation of the boundary layer in the corresponding region and produces a large number of turbulent structures. These fine turbulent structures, however, cannot be captured by the SST turbulence model.

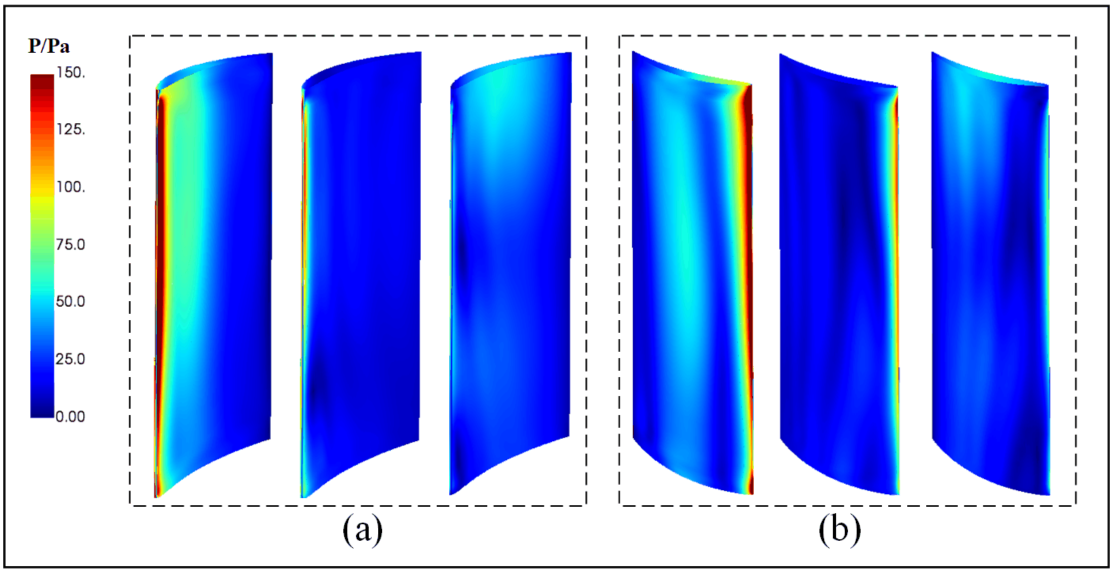

Figure 12. The distribution of the pressure amplitudes on the stator surface for the first three orders of the BPF. (a) and (b) represent the pressure and suction surfaces. In (a) and (b), the images from left to right show the distribution of the pressure amplitudes at the first-order (1400 Hz), second-order (2800 Hz), and third-order (4200 Hz) BPF.

Figure 14 shows the pressure amplitudes at the stator leading edge tip for the first three orders of the BPF, calculated for five TC configurations. Regardless of the order of the BPF, the difference in TC mainly affects the leading-edge tip area (the circled area in Figure 14).

Interestingly, the pressure amplitude at the leading-edge tip region is the highest with TC = 0 mm. When the TC is set equal to 0.25 mm, the pressure amplitude in the circled area decreases greatly. When the TC is further increased up to 1 mm, the pressure amplitude in the circled area increases. The reason for this phenomenon is that the radial separation flow and the tip leakage flow shown in Figure 10 are mixed to become the main components of the rotor wake. Without clearance, the rotor wake above the 90 span develops entirely from the radially separated flow. Once there is a gap, the radially separated flow is mixed with the tip leakage flow above the 90 span so that the strength of the rotor wake is reduced, which in turn leads to a significant reduction in the pressure amplitude in the leading-edge tip region. Further increasing the TC produces an increase in tip leakage flow intensity, which makes the rotor wake above the 90 span more intense. This increase in intensity results in a gradual augmentation of pressure pulsation in the tip region. Figure 13 also shows another general rule; the amplitude of the stator surface pressure decreases with the increase of the BPF order.

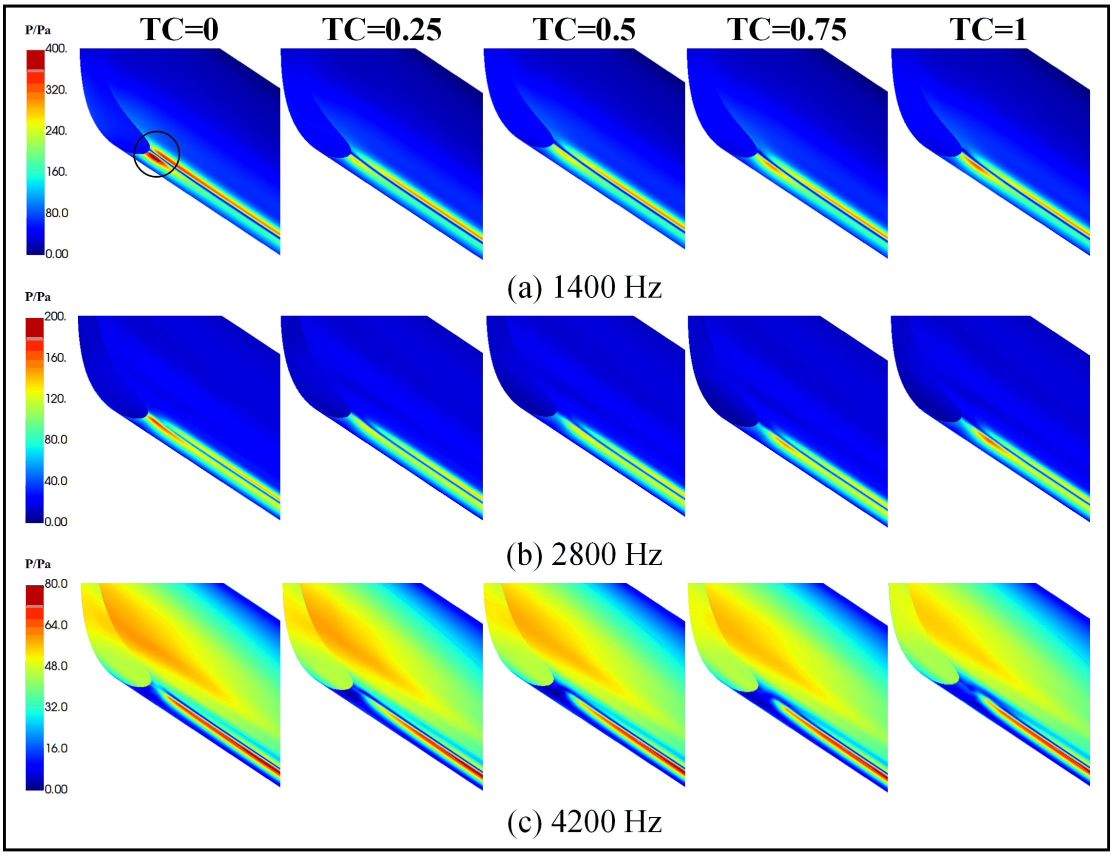

Figure 13. Pressure amplitude distribution of stator leading edge tip region for five TC configurations.

4.3 Acoustic response in a free sound field

Three field plane grids were added to observe the sound pressure response of the compressor in a free-field environment, as shown in Figure 14. The three planes were perpendicular to each other and the XY plane was perpendicular to the axial direction of the compressor. The real sound pressure distribution of the compressor with a TC of 1 mm is shown in Figure 15. The sound pressure in the XY plane at the second-order BPF is similar to that of a spherical wave radiating outward. The sound pressure distributions in the XZ and YZ planes show an obvious dipole feature. Interestingly, the dipole propagation directions of odd-order harmonics (1 and 3 BPF) are vertical, as indicated by the arrows in Figure 15(b), whereas the dipole propagation directions of even-order harmonics (2 BPF) are horizontal. The maximum sound pressure occurs at 2 BPF, which is not consistent with the results of the sound source analysis. It should be noted that a blade with a complex curved surface is composed of multiple sound sources and a large sound source in a local area does not mean that the response after the superposition of many sound sources is the largest.

Table 6. The radiated sound power for five TC configurations.

TC (mm)	0	0.25	0.5	0.75	1
1 BPF (dB)	92.8	92.4	92.4	92.3	92.2
2 BPF (dB)	104.4	103.9	103.9	103.9	103.9
3 BPF (dB)	84.7	84.6	84.5	84.3	84.2
TSP (dB)	120.2	119.7	119.7	119.7	119.7

The radiated sound power of the non-reflective spherical surface in Figure 8(a) was adopted to evaluate the effect of different TCs on the compressor-free sound field environment. Table 6 gives the sound power at the first three orders of the BPF and the total sound power (TSP). The sound power at the second-order BPF is the largest, which is consistent with the results of the sound pressure distribution. Increasing the TC from 0 to 0.25 mm causes the sound power to decrease. Upon further increase of the TC up to 1 mm causes the sound power corresponding to the first and third-order BPF to decrease, but the second-order BPF and TSP remain unchanged.

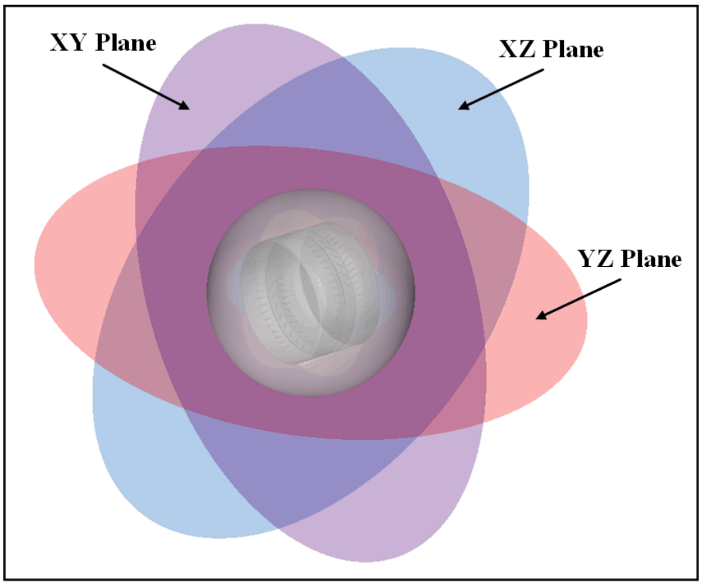

Figure 14. Three plane grid positions for the free sound field.

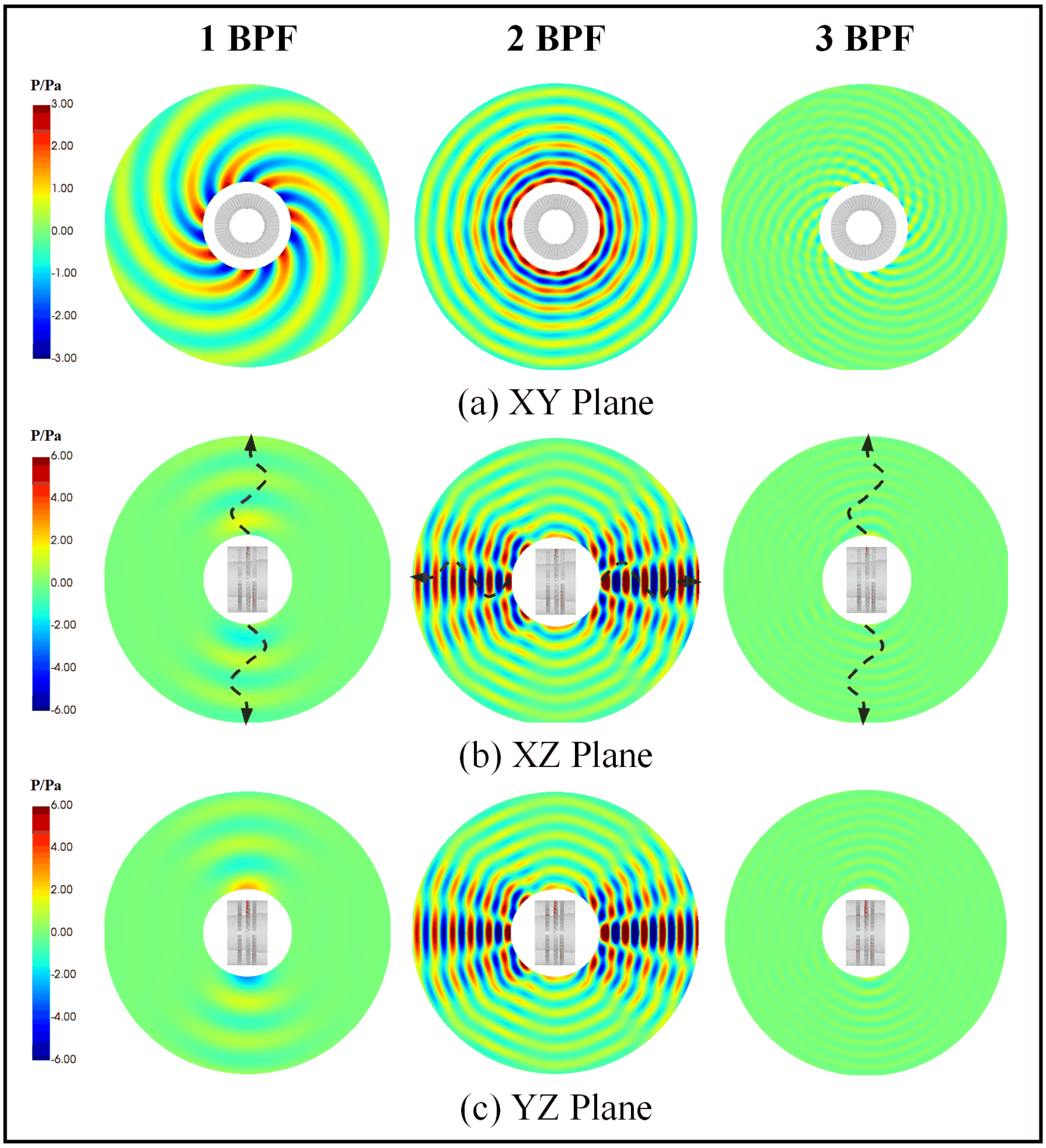

Figure 15. The real sound pressure distribution in the free-field with TC = 1 mm.

4.4 Acoustic response for an infinitely long duct

The sound pressure in the infinitely long annular pipe is shown in Figure 16. The sound pressure at the BPF is hard to propagate in the pipe and decays rapidly in a short distance. The reason for this phenomenon is inseparable from whether the annular pipe mode can propagate or not. A preliminary evaluation of the sound propagation in the pipe is obtained using

$$f_{mn} = \sqrt{1 - M^2} \frac{\alpha_{mn} c}{2\pi a} \tag{11}$$

to calculate the cut-off frequencies of the higher-order modes in an annular pipe. In Eq. (11), f_{mn} is the cut-off frequency of the m-th order circumferential and n-th order radial modes, M is the Mach number corresponding to the axial velocity, α_{mn} is the n-th zero point of the derivative of the m-th order Bessel function of the annular pipe, c is the speed of sound, and a is the outer diameter.

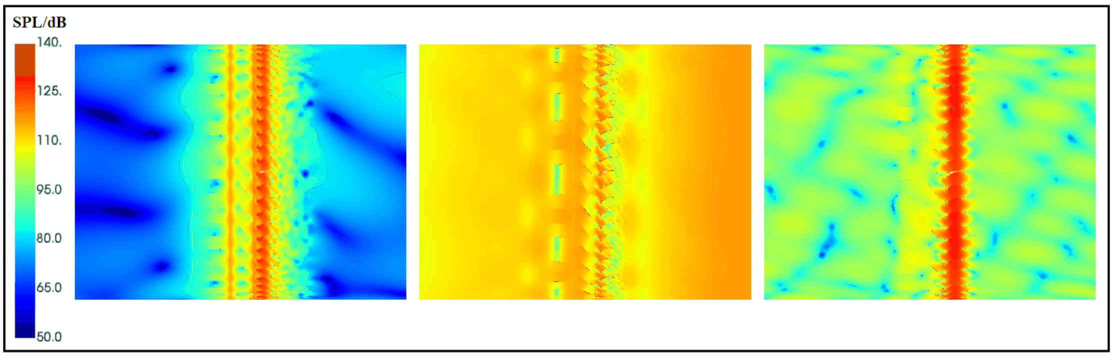

Figure 16. The first three order BPF sound pressure distribution with TC = 1 mm. The images from left to right give results for the first order (1400 Hz), second-order (2800 Hz), and third-order (4200 Hz) BPF.

Considering the axial velocity and the parameters given in Table 1, the modes and cut-off frequencies that the annular pipe can propagate at 1400 Hz are shown in Table 7. At 1400 Hz, the circumferential mode order that the annular pipe can propagate is only up to 4 and no higher-order radial modes are excited. All other higher-order modes decay at the BPF. Nevertheless, the large number of compressor blades produces circumferential modes well beyond the 4th order (Tyler and Sofrin 1962; Wang et al. 2020) and the modal results after the number of channels are simplified will be somewhat different from the full channel calculation.

Table 7. The cut-off frequency of the inlet and outlet modes.

Mode	Cut-off frequency (Hz)	
	Inlet	Outlet
(0,0)	0	0
(1,0)	311.5	294.8
(2,0)	618.4	588
(3,0)	916.9	877.8
(4,0)	1204.6	1162.8

The left and right end faces in Figure 8(b) where the reflection-free mode was applied were used to study the sound power of the compressor in an infinitely long duct. The forward and backward propagating radiated sound power was measured by the end face sound power near the guide vane and stator, respectively. The results are summarized in Tables 8 and 9. For both forward and backward noise, increasing the TC from 0 to 0.25 mm causes the sound power to decrease, which is consistent with the results obtained for the free sound field. Increasing the TC from 0.25 to 1 mm causes complex changes to the first three order BPF and the TSP increases slightly. The backward noise is generally larger than the forward noise, indicating that the noise of the compressor in the pipe is mainly propagated backward.

Table 8. The forward propagating radiated sound power for five TC configurations.

TC (mm)	0	0.25	0.5	0.75	1
1 BPF (dB)	56.8	56.8	58.4	57.2	57.6
2 BPF (dB)	96.1	95.6	95.5	95.7	95.8
3 BPF (dB)	82.0	81.7	81.7	81.7	81.7
TSP (dB)	111.7	111.2	111.2	111.3	111.4

Table 9. The backward propagating radiated sound power for five TC configurations.

TC (mm)	0	0.25	0.5	0.75	1
1 BPF (dB)	61.5	61.6	61.6	61.3	62.1

2 BPF (dB)	99.8	98.7	98.5	98.7	98.8
3 BPF (dB)	81.0	80.8	80.8	80.9	80.8
TSP (dB)	115.3	114.3	114.1	114.2	114.3

4.5 Acoustic response in the actual duct

The sound pressure distributions in the actual duct for the first three orders of the BPF are shown in Figure 17. The results are similar to those for an infinite pipe. As previously analyzed, the cut-off frequency of the compressor to generate most of the higher-order modes in the duct is well beyond 1400 Hz, so the sound pressure corresponding to the BPF decays rapidly in the pipe. The second and third-order BPF sound pressures are propagated into the far-field through the long mass flow tube.

The actual ducted exhaust volute is connected to the exhaust line and the radiated sound power at the inlet is more of a concern due to exposure to air. For the inlet arc surface shown in Figure 8(c), the sound power was calculated to characterize the acoustic laws of disparate TC in the actual environment, as shown in Table 10. Increasing the TC from 0 to 0.25 mm causes the sound power to decrease, which is consistent with the results obtained for the free sound field and the infinite duct. When the TC increases from 0.25 to 1 mm, the sound power of the first three orders of the BPF shows a gradual increase. The TSP remains largely unchanged under the three acoustic environments studied here.

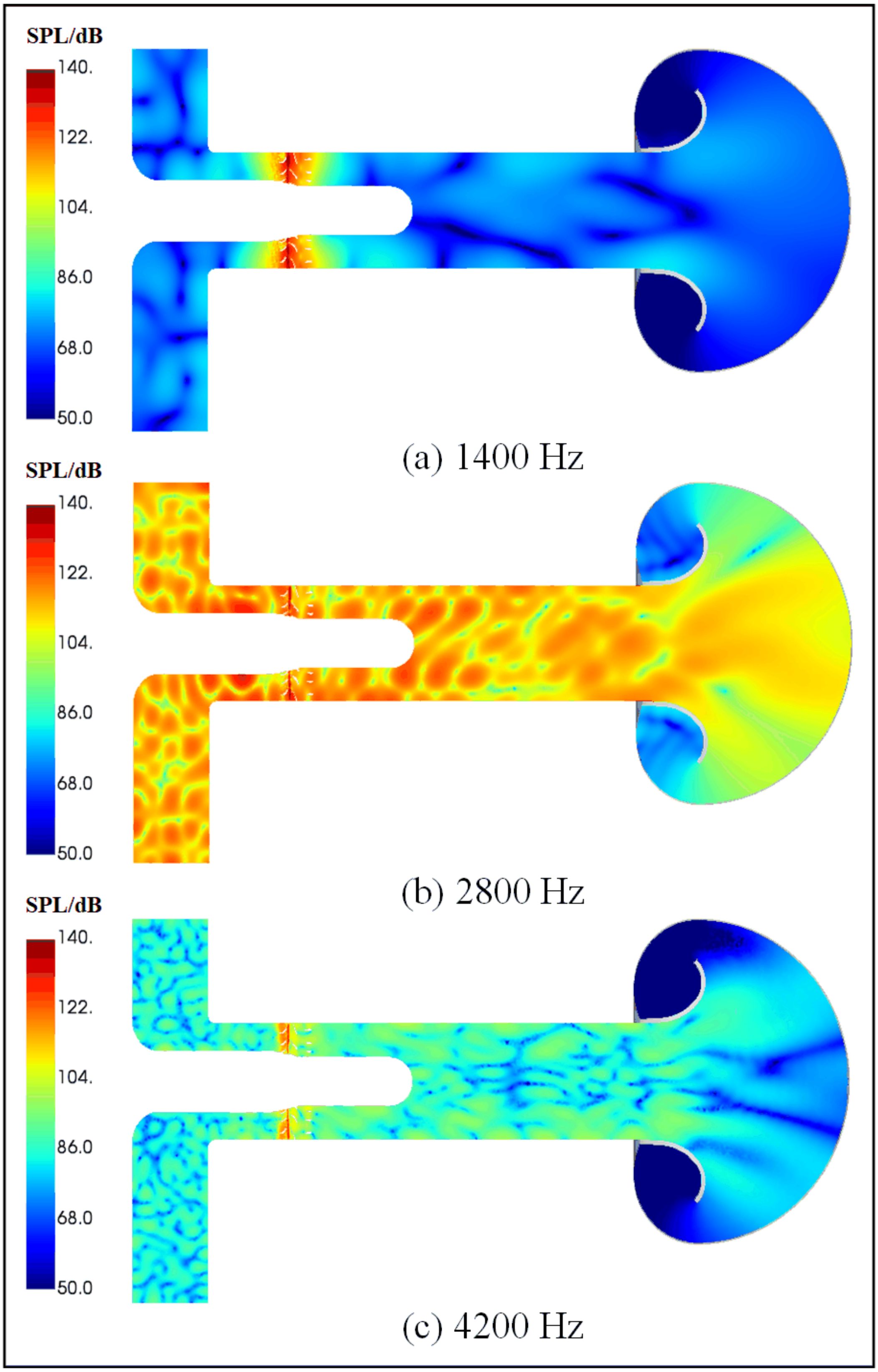

Figure 17. The first three-order BPF sound pressure distribution with TC of 1 mm in the actual duct.

Table 10. The radiated sound power from inlet for five TC configurations.

TC (mm)	0	0.25	0.5	0.75	1
1 BPF (dB)	63.1	62.7	62.6	62.7	62.6
2 BPF (dB)	98.2	98.0	98.0	98.1	98.1
3 BPF (dB)	76.3	76.1	76.3	76.6	76.6
TSP (dB)	113.7	113.4	113.5	113.6	113.6

5. Conclusions

This study combined the methods of CFD and FEM to investigate the aerodynamic and noise performance characteristics of a marine 1.5-stage compressor with five different TC configurations. The aerodynamic noise was studied in three acoustic environments, namely, in free-field, an infinitely long duct, and an actual duct. The overall characteristics of the compressor were simulated using numerical calculations and the accuracy was verified using experimental measurements. The insights garnered from this study can facilitate the advancement of noise reduction strategies in marine compressors, thereby enhancing the acoustic environment onboard ships and contributing to the overall operational efficiency and comfort of marine vessels. Consequently, this research serves as a pivotal reference for future endeavors aimed at optimizing noise control measures in the maritime domain.

Numerical analysis indicates that a large TC will induce tip leakage vortices with a larger intensity and range, which will increase the aerodynamic loss of the compressor and ultimately lead to a decrease in its efficiency. The rotor wake above the 90 span consists of two parts, the radial separation flow at the trailing edge of the blade and the tip leakage flow. When the TC increased from 0 to 0.25 mm, the rotor wake strength is reduced by the effect of blending. Further increasing the TC leads, however, to a rise in the tip leakage vortex strength and a corresponding increase in the rotor wake strength.

For the marine compressor investigated in this study, the main sound source region of the stator is the leading edge of the compressor RSI and the impact of the TC on the RSI is limited to the leading-edge region of the blade's tip. Analysis of the rotor wake showed that the pressure amplitude of the leading edge of the stator tip is the largest at TC = 0 and the configuration with TC = 0.25 mm produces the lowest sound source in the region of the leading edge of the tip. The amplitude of the stator surface pressure decreases with the order of the BPF.

For the free-field environment, the acoustic radiation of the marine compressor in the axial direction resembles a spherical wave, while in the remaining two planes it exhibits distinct dipole characteristics. Interestingly, the dipole propagation directions of odd-order harmonics and even-order harmonics are vertical and horizontal, respectively. Increasing the TC has a greater effect on the sound radiation power at the first and third-order BPF, which show a slight decrease, while the second-order BPF and the TSP are essentially unchanged.

For the infinitely long duct, it is difficult for sound waves to propagate at the BPF because most of the acoustic modes produced by the marine compressor inside the pipe are attenuated. Compressor noise is greatest with TC = 0. Increasing the TC from 0.25 to 1 mm causes complex changes to the first three orders of the BPF, whilst the TSP increases slightly. Finally, the compressor aerodynamic noise propagates mainly backward.

For the actual duct, the marine compressor noise at 1400 Hz is also hard to radiate outward through the mass flow tube. The sound power of the inlet chamber is quite consistent with the variation of the sound source with different TCs, which is caused by the mixing of the TC flow and the radially separated flow.

Acknowledgement

This work was supported by National Science and Technology Major Project（HT-J2019-Ⅱ-0013-0034）

References

Avallone F, Ragni D, Casalino D. 2020. On the effect of the tip-clearance ratio on the aeroacoustics of a diffuser-augmented wind turbine. Renewable Energy. 152:1317-1327.

Boulamatsis AM, Barlas TK, Stapountzis H. 2019. Active control of wind turbines through varying blade tip sweep. Renewable Energy. 131:25-

36.
Canepa E, Cattanei A, Mazzocut Zecchin F. 2015. Effect of the rotor–stator gap variation on the tonal noise generated by axial-flow fans. Applied Acoustics. 94:29-38.
Canepa E, Cattanei A, Zecchin FM. 2019. Leakage noise and related flow pattern in a low-speed axial fan with rotating shroud. International Journal of Turbomachinery Propulsion and Power. 4(3).
Canepa E, Cattanei AF, Mazzocut Zecchin F, Milanese G, Parodi D. 2013. Experimental study of the effect of the rotor-stator gap variation on the tonal noise generated by low-speed axial fans. 19th AIAA/CEAS Aeroacoustics Conference.
Cheng H-Y, Qiao W-Y, Wang L-F, Tong F, Wang X-N. 2019. Control of tonal noise in an axial flow fan with rotor tip clearance, stator Lean and sweep. Tuijin Jishu/Journal of Propulsion Technology. 40(2):295-306.
Corsini A, Rispoli F, Sheard AG. 2009. Aerodynamic performance of blade tip end-plates designed for low-noise operation in axial flow fans. Journal of Fluids Engineering-Transactions of the Asme. 131(8).
Du J, Lin F, Zhang H, Chen J. 2008. Numerical simulation on the effect of tip clearance size on unsteadiness in tip clearance flow. Journal of Thermal Science. 17(4):337-342.
Envia E, Huff D, Morrison C. 1996. Analytical assessment of stator sweep and lean in reducing rotor-stator tone noise. Aeroacoustics Conference.
Galindo J, Tiseira A, Navarro R, Lopez MA. 2015. Influence of tip clearance on flow behavior and noise generation of centrifugal compressors in near-surge conditions. International Journal of Heat and Fluid Flow. 52:129-139.
Ghodake D, Sanjose M, Moreau S, Henner M. 2019. Modification of noise sources by virtue of blade sweep in low speed fan. 26th International Congress on Sound and Vibration, ICSV 2019, July 7, 2019 - July 11, 2019; Montreal, QC, Canada.
Goldstein ME. 1976. Aeroacoustics. New York.
Hah C, Bergner J, Schiffer HP, Asme. 2006. Short length-scale rotating stall inception in a transonic axial compressor - Criteria and mechanisms. 51st ASME Turbo Expo 2006; May 06-11; Barcelona,

SPAIN.

Hu B-B, Ouyang H, Wu Y-D, Jin G-Y, Qiang X-Q, Du Z-H. 2013. Numerical prediction of the interaction noise radiated from an axial fan. Applied Acoustics. 74(4):544-552.

Kameier F, Neise W. 1997. Experimental study of tip clearance losses and noise in axial turbomachines and their reduction. Journal of Turbomachinery. 119(3):460-471.

Karstadt S, Hess M, Matyschok B, Pelz PF, Asme. 2010. The influence of tip clearance on the acoustic and aerodynamic characteristics of fans. ASME Turbo Expo 2010; Jun 14-18; Glasgow, SCOTLAND.

Kornilov VI. 2015. Current state and prospects of researches on the control of turbulent boundary layer by air blowing. Progress in Aerospace Sciences. 76:1-23.

Lewis D, Moreau S, Jacob MC, Sanjose M. 2022. ACAT1 fan stage broadband noise prediction using large-eddy simulation and analytical models. AIAA Journal. 60(1):360-380.

Lighthill MJ. 1952. On sound generated aerodynamically I. General theory. Proceedings of the Royal Society of London Series A Mathematical Physical Sciences. 211(1107):564-587.

Moghadam SMA, Meinke M, Schroeder W. 2019. Numerical analysis of the acoustic field of a ducted axial fan at varying tip clearances. Acta Acustica United with Acustica. 105(1):43-55.

Oberai AA, Roknaldin F, Hughes TJR. 2000. Computational procedures for determining structural-acoustic response due to hydrodynamic sources. Computer Methods in Applied Mechanics and Engineering. 190(3-4):345-361.

Oberai AA, Roknaldin F, Hughes TJR. 2002. Computation of trailing-edge noise due to turbulent flow over an airfoil. AIAA Journal. 40(11):2206-2216.

Polacsek C, Burguburu S, Redonnet S, Terracol M. 2006. Numerical simulations of fan interaction noise using a hybrid approach. AIAA Journal. 44(6):1188-1196.

Sanders MP, de Santana LD, Venner CH. 2020. The sweep angle effect on slat noise characteristics of the 30P30N high-lift model in an open-jet wind tunnel. AIAA Aviation 2020 Forum.

Shi M-S, Chi P-A, Chen W-L. 2019. Prediction on turbomachinery flows using advanced turbulence models. Journal of Aeronautics, Astronautics and Aviation. 51(2):159-170.

Tong F, Qiao W, Xu K, Wang L, Chen W, Wang X. 2018. On the study of wavy leading-edge vanes to achieve low fan interaction noise. Journal of Sound and Vibration. 419:200-226.

Tyler JM, Sofrin TG. 1962. Axial flow compressor noise studies. Transactions of the Society of Automotive Engineers. 70:309-332.

Wang L, Xiang K, Mao L, Tong H, Qiao W. 2020. Numerical simulation of the effect of the tip clearance flow on rotor-stator interaction tone noise in axial-flow fan. ASME Turbo Expo 2020: Turbomachinery Technical Conference and Exposition, GT 2020, September 21, 2020 - September 25, 2020; Virtual, Online.

Yang J, Wu H. 2014. Explicit coupled solution of two-equation k- SST turbulence model and its application in turbomachinery flow simulation. Hangkong Xuebao/Acta Aeronautica et Astronautica Sinica. 35(1):116-124.

Yang Y, Liu Y, Hu H, Liu X, Wang Y, Arcondoulis EJG, Li Z. 2020. Experimental study on noise reduction of a wavy multi-copter rotor. Applied Acoustics. 165.

Zhang B, Mao X, Wu X, Liu B. 2021. Effects of tip leakage flow on the aerodynamic performance and stability of an axial-flow transonic compressor stage. Energies. 14(14).

Zhang C, Ji L, Zhou L, Sun S. 2020. Effect of blended blade tip and winglet on aerodynamic and aeroacoustic performances of a diagonal fan. Aerospace Science and Technology. 98.

Zhang C, Ji L, Zhou L, Zhang Z. 2020. Effects of different blended blade tip and winglets on aerodynamic and aeroacoustic performances of diagonal fans. Aerospace Science and Technology. 106.

Zhang H, Deng X, Chen J, Huang W. 2005. Unsteady tip clearance flow in an isolated axial compressor rotor. Journal of Thermal Science. 14(3):211-219.

Zhang J, Chu W, Zhang H, Wu Y, Dong X. 2016. Numerical and experimental investigations of the unsteady aerodynamics and aero-acoustics characteristics of a backward curved blade centrifugal fan. Applied Acoustics. 110:256-267.

Zhang M, Li J, Dong X, Sun D, Sun X. 2021. Experimental study on different tip clearance of low-speed axial fan. ASME Turbo Expo 2021: Turbomachinery Technical Conference and Exposition, GT 2021, June 7, 2021 - June 11, 2021; Virtual, Online.

Zhang W, Wang X, Sun X. 2017. Passive control of fan noise by vane sweep and lean. Hangkong Xuebao/Acta Aeronautica et Astronautica Sinica. 38(2).

Zhu T, Carolus TH. 2018. Axial fan tip clearance noise: Experiments, Lattice-Boltzmann simulation, and mitigation measures. International Journal of Aeroacoustics. 17(1-2):159-183.

Zhu T, Lallier-Daniels D, Sanjose M, Moreau S, Carolus T. 2018. Rotating coherent flow structures as a source for narrowband tip clearance noise from axial fans. Journal of Sound and Vibration. 417:198-215.